Geophysical Research Letters®

Key Points:
- First estimates of radar attenuation in the shallow Martian subsurface are on average −2.6 dB/m at the Radar Imager for Mars' Subsurface Exploration (RIMFAX) 675 MHz center frequency
- Results are consistent with magmatic lithologies on the Jezero Crater Floor
- The centroid frequency-shift method is adequately implemented for RIMFAX analysis

Correspondence to:
S. Eide,
sigurd.eide@its.uio.no

Radar Attenuation in the Shallow Martian Subsurface: RIMFAX Time-Frequency Analysis and Constant-Q Characterization Over Jezero Crater Floor

Sigurd Eide[1] [ID], **Titus M. Casademont[1]** [ID], **Tor Berger[1,2]**, **Henning Dypvik[1]**, **Emileigh S. Shoemaker[3]** [ID], and **Svein-Erik Hamran[1]**

[1]Centre for Space Sensors and Systems (CENSSS), University of Oslo, Kjeller, Norway, [2]Norwegian Defence Research Establishment (FFI), Kjeller, Norway, [3]Lunar and Planetary Laboratory, University of Arizona, Tucson, AZ, USA

Abstract Attenuation of radar waves in the subsurface can be quantified with a constant-Q approximation through time-frequency analysis. We implement the centroid frequency-shift method and study Radar Imager for Mars' Subsurface Exploration (RIMFAX) data acquired along the Mars 2020 Perseverance rover traverse. Attenuation is among key media properties, but quantified estimates need to account for instrument characteristics and limitations in the analysis technique. We ensure accurate constant-Q characterization and present the first estimates of radar attenuation in the upper 5 m of the shallow Martian subsurface. Over Jezero Crater Floor, constant-Q is on average 70.4 ± 7.7, which equals an attenuation of −2.6 ± 0.3 dB/m at RIMFAX' 675 MHz center frequency. Regions comprising the Máaz or Séítah formations have similar attenuation properties that are consistent with magmatic lithologies.

Plain Language Summary First estimates of radar attenuation in the shallow Martian subsurface are presented. Estimates are from Jezero Crater Floor, along the drive path of the Mars 2020 Perseverance rover. Attenuation is among key media properties that describe radar wave propagation and can relate to lithological properties. Estimates of signal losses are consistent with magmatic lithologies and differences between distinct regions on Jezero Crater Floor are not detected.

1. Introduction

During the first 379 sols of NASA's Perseverance rover mission on Mars, over 5 km had been driven over the Jezero Crater Floor. The rover had gone from the Octavia E. Butler landing site (OEB), located on the relatively flat terrain of the Máaz Formation, to the distinct rugged exposures of the Séítah Formation. Afterward, the rover drove back again to OEB, largely backtracking its original route. The Radar Imager for Mars' Subsurface Exploration (RIMFAX; Hamran et al., 2020) conducted measurements along the whole traverse, providing an exceptional data set for constraining subsurface parameters over a large geographical area spanning several different regions (Figure 1). Moreover, the close vicinity of the two passes allows for testing replicability of obtained media parameters.

The first look into the shallow Martian subsurface disclosed intriguing reflector geometries, which at places can be correlated with outcropping rock formations on the surface (Hamran et al., 2022). Yet, more information is contained in the acquired data, hidden by randomly distributed reflections dominating the radar image. This calls for supplementary analysis of the radar data beyond that of visual inspection.

Ground-penetrating radar (GPR) data is strongly affected by the frequency dependent attenuation mechanisms. In general, higher frequency content is attenuated more than lower, so that subsurface reflection spectra will be altered compared to that of the transmitted waveform. The constant-Q factor was originally used to describe similar behavior of seismic waves due to cumulative attenuating effects in the ground (Richards & Aki, 1980), but it has also been found applicable for electromagnetic propagation in natural soil and rocks over the GPR frequency range 0.1–1.0 GHz (Harbi & McMechan, 2012; Turner & Siggins, 1994). For this reason, it can be appropriate to assume a linear frequency dependence for the attenuation in GPR sounding:

$$E(\omega, t_{twt}) = E_0(\omega) \times \exp\left(-\frac{\omega t_{twt}}{2Q^*}\right). \tag{1}$$

Supervision: Tor Berger, Henning Dypvik
Validation: Sigurd Eide
Visualization: Sigurd Eide, Svein-Erik Hamran
Writing – original draft: Sigurd Eide
Writing – review & editing: Sigurd Eide, Titus M. Casademont, Henning Dypvik, Emileigh S. Shoemaker

The frequency spectrum of the electric field intensity $E(\omega, t_{twt})$ is a function of angular frequency ω and propagation time t_{twt}. $E_0(\omega)$ is the spectrum of the transmitted waveform. Turner and Siggins (1994) noted that the GPR parameter Q* is effectively a generalized version of the corresponding seismic parameter Q, but differs as radar attenuation extrapolates to a finite value at zero frequency. However, this difference bears little practical significance in radargram analysis of low conductivity media like the dry Martian regolith. From evaluating the exponential term in Equation 1, the attenuation constant α can be written in terms of Q* and the propagation velocity v:

$$\alpha = \frac{\omega}{2Q^* v} \; [Np/m] = 8.69 \times \frac{\omega}{2Q^* v} \; [dB/m].$$

(2)

In many radar studies, the relationship between the imaginary and real part of a dielectric model is commonly described by the loss tangent (tanδ). For non-dispersive media and in the absence of scattering losses, it will effectively be the inverse Q*-factor. In fact, the "universal" power-law that approximates media permittivity above the relaxation frequency (Jonscher, 1977), implies a constant-Q model (Bano, 1996). Bradford (2007) also show how the constant-Q model is useful for describing several dielectric models, like Cole-Cole or Debye, in the case of band-limited GPR signals.

In addition to dielectric attenuation, volume scattering losses are frequency dependent and contribute to the composite signal attenuation, for example, Mie scattering by idealized distribution of spherical inclusions (e.g., Ulaby & Long, 2014) or layer scattering as predicted by localization theory (Van Der Baan, 2001). For GPR field measurements, the constant-Q model has proven useful for describing the bulk attenuation (Bradford, 2007; Ding et al., 2020; Economou & Kritikakis, 2016; Irving & Knight, 2003; Lauro et al., 2022). Moreover, radars in orbit around Mars also assume a constant-Q equivalent model (B. Campbell & Morgan, 2018; B. Campbell et al., 2008). The term "effective loss tangent" is sometimes used for describing bulk attenuation (tan$\delta_e = 1/Q^*$).

There exist numerous techniques for estimating the Q*-factor (e.g., Tonn, 1991). As relative change in spectral components is independent of the total signal strength at a certain time interval, spectral methods are especially suitable for recordings where true amplitudes are not easily retrieved. In this study, we study both spectra of selected reflections and the integrated time-frequency (T-F) spectra of whole radargram sections. By doing so, we omit having to correct for numerous RIMFAX acquisition parameters in order to adjust and calibrate amplitudes. For a monostatic radar such as RIMFAX, reflection amplitudes along a natural subsurface target will furthermore vary greatly with the viewing angle and variation in media properties, which makes amplitude analysis challenging.

The centroid-frequency shift (CFS) method (Quan & Harris, 1997) is employed to obtain constant-Q estimates in RIMFAX data. We investigate if we can obtain reliable Q*-factor estimates and if it is possible to detect any significant variation over Jezero Crater Floor. The CFS technique's accuracy is one aspect that previously has not been evaluated thoroughly. Through a numerical modeling experiment, we ensure an appropriate implementation of the analysis and study the accuracy of the method. Processing steps needed for preparing RIMFAX data for spectral analysis are also addressed. Thereafter, the first estimates of radar attenuation in the upper 5 m of the Martian subsurface are presented.

2. Methods

In this section we first review the centroid frequency-shift (CFS) technique for determining the Q*-parameter. A numerical modeling experiment will then be used to ensure a correct implementation of the CFS technique and to assess the accuracy of the analysis. Finally, a spectral enhancement processing step will be implemented, which is needed for preparing RIMFAX' frequency modulated continuous wave (FMCW) radar data for spectral analysis.

2.1. Spectral Analysis and the Centroid Frequency-Shift Method

Quan and Harris (1997) present the CFS method where the Q*-factor is obtained analytically from the slope $\Delta f_c / \Delta t_{twt}$ in a recording:

$$Q^* = -C\pi \left(\frac{\Delta f_c}{\Delta t_{twt}} \right)^{-1}.$$
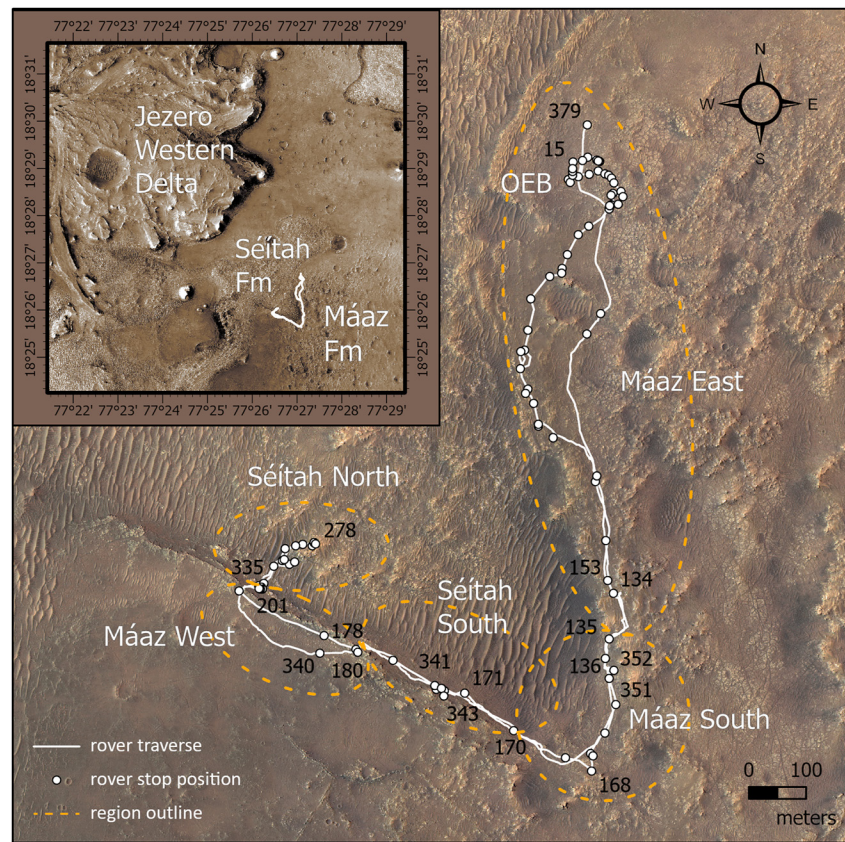
(3)

Figure 1. Map view over RIMFAX soundings conducted while driving over the Crater Floor. Inset figure gives the large-scale perspective and show the location of the rover traverse with regards to the Jezero Western Delta. During the first 379 sols, the rover drove from OEB to Séítah, and back. In the map are orange dashed ellipses outlining distinct regions that are investigated separately in this study: (i) Máaz East (sol 15–135 and 353–379); (ii) Máaz South (sol 136–170 and 351–353); (iii) Séítah South (sol 171–178 and 341–351); (iv) Máaz West (sol 180–201 and 340–341); and (v) Séítah North (sol 201–278 and 280–335). Basemaps are Mars 2020 Science Team colored HiRISE mosaics.

The instantaneous center frequency f_c is evaluated over travel time t_{twt}. The constant C depends on the waveform shape and bandwidth, which for a Gaussian waveform equals its variance (in Hz). The amplitude taper employed during FMCW radar processing ideally decides the radar system's impulse response, that is, the waveform equivalent, and enables accurate determination of C and direct use of the equation.

There are several approaches for obtaining the CFS in a single trace or in a section of a radargram. Here we employ the Short-Time Fourier Transform (STFT) to obtain the integrated time-frequency (T-F) spectra of several neighboring traces. For a Gaussian amplitude taper applied during processing over the signal's bandwidth, the instantaneous center frequency will be at the spectra's peak magnitude, for a given travel time. At 1.5 ns time increments in the STFT spectra, the central frequency is identified as the midpoint between −6 dB below the peak spectral value. Then, the slope of the CFS is obtained from a least-square linear regression of central frequencies with travel time.

The CFS can also be obtained from analyzing a coherent reflection in a radargram. A Fourier Transform of a selection with only the target reflection, will ideally give the frequency content of that individual reflection. Doing this on traces where the reflection is located at varying depth, the CFS can be obtained by a linear regression of center frequencies with travel time.

2.2. Evaluation of Analysis Method on Synthetic Data

To assess the CFS technique, we model the radar response over a subsurface model for a range of different Q-values. The subsurface model in Figure 2a is from Eide et al. (2022), consisting of a layered medium overlying
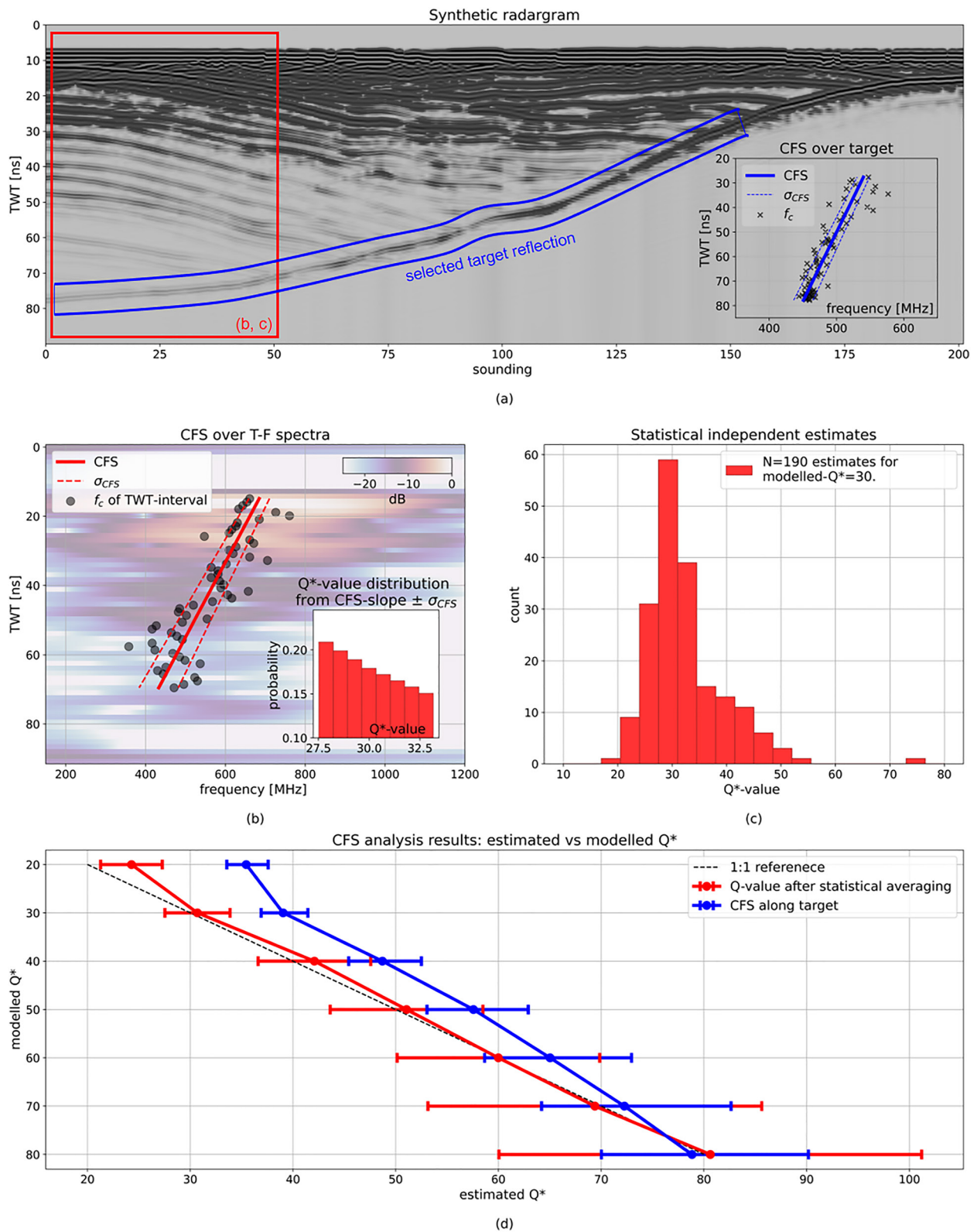
Figure 2.

a strong target reflection. For each simulation, layers have the same given Q-value and permittivities around a mean of $\varepsilon' = 6$. Soundings are simulated at 0.1 m intervals along a 20 m transect. Numerical simulations are conducted with gprMax (Warren et al., 2016) with the dielectric constant-Q model implemented through a multiple pole Debye formulation (Giannakis & Giannopoulos, 2014). Corrections according to Eide et al. (2022) are applied to the simulation results, in order to replicate a FMCW radar with the same bandwidth and central frequency as RIMFAX. Corrections imitate FMCW radar processing with a Gaussian-shaped amplitude taper.

Analyzing the synthetic radargram in Figure 2a should be a suitable numerical experiment for evaluating the spectral analysis methods for RIMFAX data. Note, during analysis of the synthetic data, the surface reflection is removed as in Eide et al. (2022) for improved imaging of subsurface structures. The target analysis is focused on the reflection within the blue selection, while the integrated T-F spectra analysis focuses on the red selection. Inset figure shows the CFS fit for the target, with the standard deviation of the residuals as an estimate of the uncertainty.

Results from the CFS analysis are highly sensitive to the linear fit to the center frequencies, so a statistical approach was taken for the T-F spectra analysis. Figure 2b displays the regression to the estimated center frequencies of each time interval in the T-F spectra. The inset figure shows the range of Q*-values within one standard deviation of the residuals ($\pm\sigma_{CFS}$). As the function Q* has an hyperbolic dependence with the slope $\Delta f/\Delta t_{twt}$, valid (positive) Q* estimates will be drawn from an exponential distribution. That is, small inaccuracies during slope regression will not yield Q* estimates centered around the true Q* value in the data. But an improved estimate can be obtained by averaging statistically independent estimates, which will result in a more centralized distribution. The statistically independent estimates are obtained by conducting CFS fits to multiple selections of neighboring soundings within the analyzed radargram section. With the skewed distribution in (c), the median of all estimated Q*-values is the most likely and the uncertainty is defined in terms of the semi-interquartile range (semi-IQR).

Conducting the same target and T-F spectra analyses for models with Q*-values between 20 and 80, we obtain the results in (d). The accuracy of the target analysis in blue is low for modeled Q*-values of 60 and less, but consistent in that models with lower Q*-factors results in lower Q*-estimates. For analysis of the T-F spectra, a better match with the modeled Q* is obtained. The statistical approach clearly helps constraining the average value. Still, it can be observed that the analysis results have high uncertainties that increase with higher Q*-values.

2.3. Spectral Enhancement of RIMFAX' Deramped Signal

This study analyses RIMFAX' shallow mode recordings acquired across the full bandwidth, 150–1,200 MHz. RIMFAX is a stretch processing receiver that records a deramped signal from the mixer output (see Eide et al., 2022; Hamran et al., 2020). The first processing step is a background removal (BGR) with a single value decomposition filter, applied to remove ringing in the recording. Figures 3a–3d present the raw and filtered deramped signal.

In (e, f) an amplitude taper is applied, for sidelobe reduction in the later Fourier transform and radargram generation. For the CFS analysis, a Gaussian window was selected with a standard deviation equal 20% of the bandwidth (122 sweep time samples). For a Gaussian window centered at the 675 MHz RIMFAX center frequency, that is equivalent to 210 MHz. When conducting spectral analysis, there is a trade-off between a well-represented Gaussian function (small standard deviation) and a wide bandwidth for better constrain on the CFS (large standard deviation). The selected window was seen to work well over RIMFAX' bandwidth.

In some of RIMFAX' sweep time samples, the signal is dominated by artifacts after BGR. Samples between 250 and 300 are influenced by a combination of (a) low synthesized signals in the electronic box over that interval, (b) low antenna gain at the corresponding frequencies, and (c) noticeable strong ringing occurring during that time of the FMCW sweep. This results in a radargram having non-uniform frequency spectrum with certain

Figure 2. CFS analysis on synthetic data modeled with constant-Q dielectric media. (a) Synthetic radargram with selection in red for the integrated T-F analysis and selection in blue for target reflection analysis. Inset figure shows the scatter plot of the target's center frequencies for each sounding, and the CFS linear regression. Error bars are according to the standard deviation of the residuals in the regression (σ_{CFS}). The analysis is illustrated in the case of a model with Q* = 30. (b) CFS linear regression over T-F spectra in the case of Q* = 30. Inset figure show the exponential distribution of values within one standard deviation of the regression residuals ($\pm\sigma_{CFS}$), illustrating the low accuracy of a single CFS regression. (c) A statistical averaging is done to overcome the low accuracy in a single T-F CFS regression, with the median of N statistically independent estimates providing a more reliable results. (d) Results form integrated spectra and target analyses for modeled Q*-values in the range 20–80. Error bars for the statistically averaged T-F spectra estimates are according to the semi-IQR.
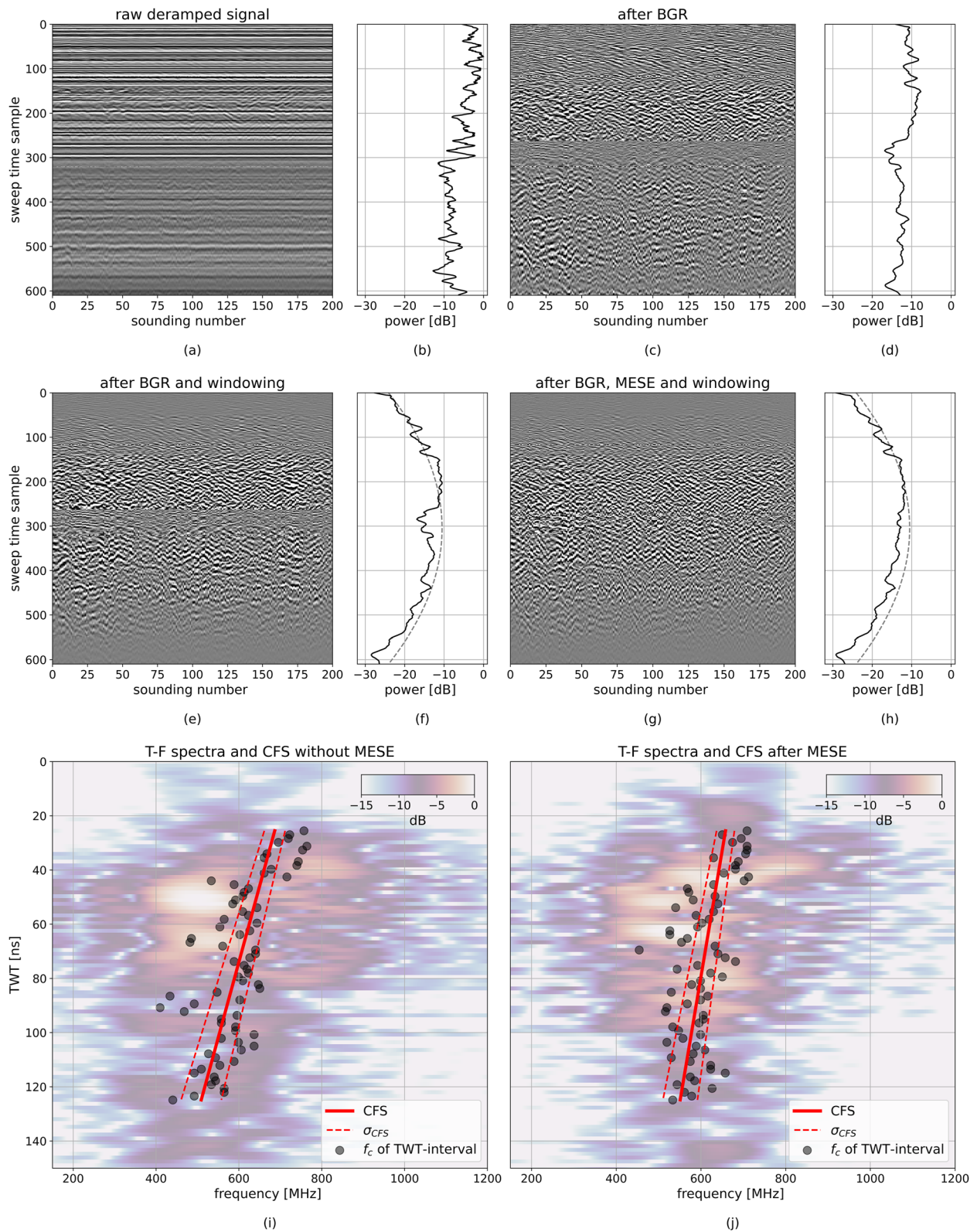
Figure 3.

low-magnitude bands dominated by artifacts. For layer detection, this is not crucial as a Fourier transform of the deramped signal will still retrieve targets' time-delays. When studying spectral characteristics of the signal, however, this can deteriorate the analysis.

The deramped signal, in theory, is composed of series of superimposed monochromatic waves, whose frequencies correspond to targets' travel time delays. We therefore make the fundamental assumption that it is possible to mute and interpolate over the samples that cannot properly be retrieved, in order to reconstruct the original signal content. A range of techniques exists for wavefield reconstruction with, for example, recent advances employing convolutional neural network approaches (Larsen Greiner et al., 2020). Still, the autoregressive maximum entropy method (Burg, 1975) remains a viable option for predicting missing parts of a signal based on preceding or proceeding data points. It has, for example, had successful application in bandwidth extrapolation for radar systems (Gambacorta et al., 2022; Oudart et al., 2021). The reconstructed signal over an interval of removed samples, will be a linear combination of the changes above and below in each recorded signal. This is consistent with the linear assumption of a constant-Q model.

Figures 3e–3h compare the windowed deramped signal without and after Maximum Entropy Spectral Enhancement (MESE). The sample range 250–300 in (e), has been improved to a more consistent image in (g). These samples are also seen as a dip in the integrated power spectra in (f), while in (h) a more even power spectra has been retrieved. By applying MESE, the results after windowing will be more aligned with the expected performance of the window function, and hence help improve spectral analysis of RIMFAX data.

A Fourier transform of the deramped signal will yield the radargram, and a STFT of the radargram will generate the T-F spectra. In (i, j) are the T-F spectra without and after MESE. Center frequencies at 1.5 ns time intervals and the CFS regression are also plotted over the spectra. MESE results in a more uniform spectra in (j) with center frequencies more aligned compared to the spectra in (i). The CFS analysis is limited to the time range 25–125 ns, corresponding to the first 100 ns below the surface reflection. Beyond that recording time, RIMFAX shallow mode spectra can be dominated by noise. For the average subsurface radar wave velocity in Jezero Crater of 0.1 m/ns (Casademont et al., 2023), 100 ns corresponds to a depth of 5 m.

3. Results and Discussion

Based on the modeling experiment, we conclude that T-F spectra analysis is more appropriate compared to target analysis. T-F spectra are more suitable for a statistical averaging implementation, which improves accuracy. Its automated implementation is also better suited for processing the large amount of data acquired along the entire rover traverse. Moreover, RIMFAX radargrams are dominated high-amplitude reflection packages instead of single coherent reflections (Hamran et al., 2022), making target picking ambiguous.

Results form T-F CFS analysis every 10 m along the rover traverse are presented in Figure 4. The average for the whole Jezero Crater Floor is in (a) while (b–f) cover the five regions in Figure 1 individually. In (b–f), separate estimates are made for the OEB-Séítah and Séítah-OEB passes. The difference between mean values of two passes within a single region, is comparable to differences between regions. Moreover, all regions have mean values close to the combined estimate in (a), which for all soundings over the Crater Floor is $Q* = 70.4 \pm 7.7$. At the RIMFAX 675 MHz center frequency, that equates to an attenuation of -2.6 ± 0.3 dB/m assuming a subsurface velocity of 0.1 m/ns (Casademont et al., 2023). Uncertainties are listed in terms of standard deviations. In terms of the effective loss tangent, the average estimate equals $\tan\delta_e = 0.014 \pm 0.002$.

That attenuation is similar over the Jezero Crater Floor, is in line with results from Hamran et al. (2022) where maximum imaging depths are fairly constant. Casademont et al. (2023) analyzed dielectric permittivity in the RIMFAX data and found only small differences between regions. Similar propagation velocities and similar attenuation estimates, could indicate that the shallow subsurface electrical properties are comparable over the whole investigated area. Simultaneously, it may reflect limitations in the analyses' accuracy.

Figure 3. Example of RIMFAX' deramped signal and the effect of MESE. (a) The raw recorded deramped signal for 200 soundings and (b) the corresponding average power spectrum. (c, d) The deramped signal and its power spectrum after BGR. After ringing is removed, the signal level drops to about −10 dB below the raw data recording. Low magnitude sweep time samples appears in the range 250–300. (e, f) The deramped signal after applied amplitude taper, or windowing. (g, h) The windowed deramped signal after applied MESE. The window function is Gaussian with a standard deviation of 20% of the bandwidth, and is shown in (f, h) with a dashed gray line. After MESE in (g), low magnitude samples have been improved, and in (h) the power spectra is more aligned with the window function. (i, j) STFT spectra without and after MESE. Estimated center frequencies f_c align better after MESE and improve the CFS linear regression.
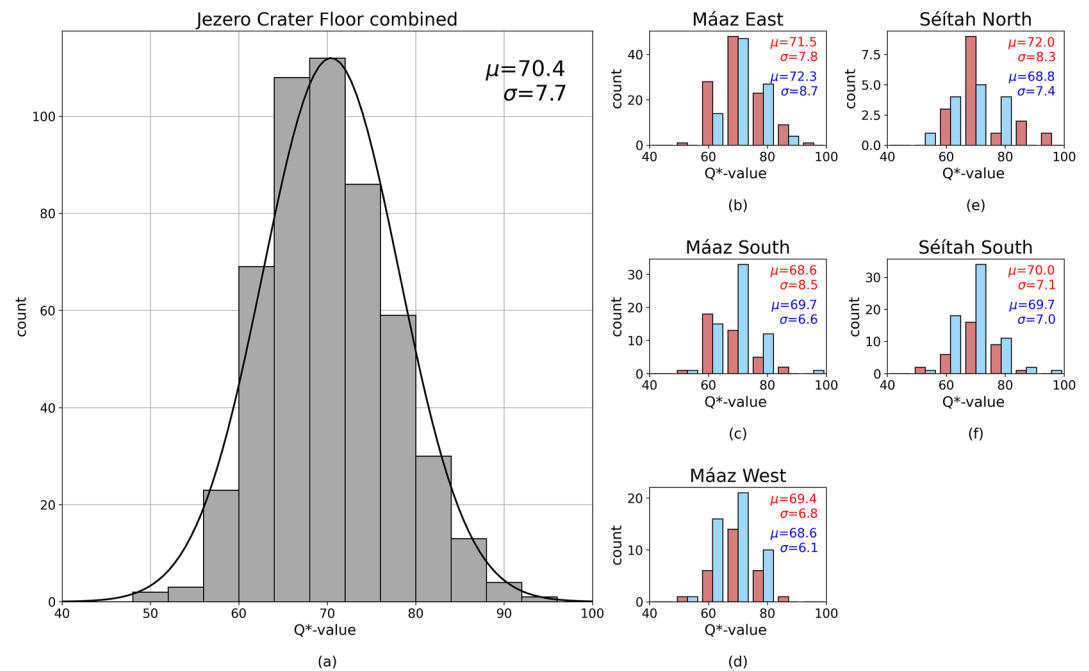
Figure 4. Results form CFS analysis of T-F spectra every 10 m from sol 15 to 379. (a) Histogram of the combined results together with a Gaussian distribution fit. (b–f) The analysis divided into five regions comprising either a part of the Máaz or Séítah formations: (b) Máaz East; (c) Máaz South; (d) Máaz West; (e) Séítah North; and (f) Séítah South. For each separate region, parts of drives extending beyond its boundary are not included in the analysis. Passes are analyzed separately, colored in red for OEB-Séítah and blue for Séítah-OEB. The mean value (μ) and its standard deviation (σ) are listed with each histogram.

Still, Casademont et al. (2023) inferred a small increase in permittivity and density going from the Máaz to Séítah Formation, which was also concluded from observations by the SuperCam instrument of outcrops on the surface (Wiens et al., 2022). The stratigraphic order between Séítah and Máaz was disclosed by RIMFAX imaging (Hamran et al., 2022), but their exact relationship and true emplacement histories are currently under debate (Farley et al., 2022). It is not understood whether (a) Máaz is a separate lithology emplaced on top of Séítah, or (b) if it is an upper differentiated section of the proposed Séítah igneous cumulate. The attenuation analysis, however, cannot detect any variation between the formations or discriminate between the two formation scenarios.

The constant-Q approximation generalizes the composite attenuation of electromagnetic waves and comprises both dielectric and scattering losses. Separating the two is not easily done without additional measurements, though an approach by Harbi and McMechan (2012), for example, attempts this based on theoretical models of the intrinsic losses. Water is in general dominating attenuation in natural terrains on Earth (e.g., Ulaby & Long, 2014). On the Moon, attenuation is usually ascribed to high concentrations of TiO_2 and FeO minerals (e.g., Ding et al., 2020; Olhoeft & Strangway, 1975), often disregarding subsurface volume scattering altogether. It is unknown to what extent volume scattering, mineralogy and any potential water content do affect the attenuation of radar signals in the Martian subsurface. There is furthermore an enrichment of magnetic materials on the surface of Mars (e.g., Madsen et al., 2009) that could impact attenuation in radar sounding, though Stillman and Olhoeft (2008) advocate it would be negligible based on laboratory measurements.

The orbital Martian radar SHARAD did experience a surprising absence of signal returns at places, implying high attenuation over older volcanic lithologies (>1 Ga) and over terrain inferred to have been altered by water. Scattering or bound water in clay-rich lithologies, have been proposed as possible governing loss mechanisms (Stillman & Grimm, 2011). Attenuation estimates by orbital radars, however, are not directly relatable RIMFAX, as scattering losses for wavelengths at which they operate would be caused by inhomogeneities at much larger spatial scales. Furthermore, low-frequency bound-water attenuation would be less at the RIMFAX bandwidth compared to the lower range at which SHARAD operate. But if we assume the obtained constant-Q model from this study can be extrapolated to the SHARAD 20 MHz center frequency, a Q* = 70 equals 0.08 dB/m for a

subsurface velocity of 0.1 m/ns. This estimate is toward the lower bound of the 0.065–0.27 dB/m range obtained in high attenuation regions by Stillman and Grimm (2011), but within range 0.05–0.16 dB/m of other measurements of Martian basalts (Carter et al., 2009; Simon et al., 2014).

Attenuation estimates from this study fall within range of typical values for laboratory measurements of dry magmatic lithologies (M. J. Campbell & Ulrichs, 1969; Ulaby et al., 1990), as RIMFAX permittivity estimates also do (v). Therefore, radar attenuation estimates are consistent with the interpretations by Farley et al. (2022), synthesized from both surface and subsurface observations of Jezero Crater Floor lithologies.

4. Conclusions

The attenuation for RIMFAX soundings over Jezero Crater Floor is estimated to $Q* = 70.4 \pm 7.7$, or -2.6 ± 0.3 dB/m at the 675 MHz center frequency. Regions comprising the Máaz or Séítah formations have similar attenuation properties that are consistent with magmatic lithologies. Results from this study are non-conclusive with regards to the disputed formation and emplacement histories of the Máaz and Séítah formations.

The centroid frequency-shift (CFS) technique for analyzing radar attenuation is a capable approach that bypass obstacles associated with studying returned signal power. In particular, it is applicable for FMCW radars where the amplitude taper can be appropriately selected for the spectral analysis. The accuracy of the CFS method is assessed through numerical modeling, concluding that single estimates are not reliable and statistical averaging is necessary.

Attenuation estimates from this study could be used as a starting point for more detailed quantitative studies. The results can be valuable as independent and complementary estimates for future studies of returned power in the RIMFAX data. Detailed studies could, for example, focus on smaller-scale detection of radar facies with either high- or low-$Q*$. If the shallow Martian subsurface contains liquid subsurface brines or significant amounts of bound-water bearing clays, it may be possible to detect a locally increased attenuation and a low-$Q*$. However, interpretation of attenuation is inherently non-unique with regards to scattering losses verses conductive and dielectric losses. Future work on disentangling the different loss mechanisms will therefore require additional observations or, perhaps, incorporation of appropriate attenuation models based on scientific ingenuity.

Data Availability Statement

The data used in this work are available at the NASA PDS Geosciences Node (https://pds-geosciences.wustl.edu/missions/mars2020/rimfax.htm) (Hamran & Paige, 2021).

References

Bano, M. (1996). Constant dielectric losses of ground-penetrating radar waves. *Geophysical Journal International*, *124*(1), 279–288. https://doi.org/10.1111/j.1365-246x.1996.tb06370.x

Bradford, J. H. (2007). Frequency-dependent attenuation analysis of ground-penetrating radar data. *Geophysics*, *72*(3), J7–J16. https://doi.org/10.1190/1.2710183

Burg, J. P. (1975). *Maximum entropy spectral analysis*. Stanford University.

Campbell, B., Carter, L., Phillips, R., Plaut, J., Putzig, N., Safaeinili, A., et al. (2008). Sharad radar sounding of the vastitas borealis formation in amazonis planitia. *Journal of Geophysical Research*, *113*(E12), E12010. https://doi.org/10.1029/2008je003177

Campbell, B., & Morgan, G. A. (2018). Fine-scale layering of Mars polar deposits and signatures of ice content in nonpolar material from multiband sharad data processing. *Geophysical Research Letters*, *45*(4), 1759–1766. https://doi.org/10.1002/2017gl075844

Campbell, M. J., & Ulrichs, J. (1969). Electrical properties of rocks and their significance for lunar radar observations. *Journal of Geophysical Research*, *74*(25), 5867–5881. https://doi.org/10.1029/jb074i025p05867

Carter, L. M., Campbell, B. A., Holt, J. W., Phillips, R. J., Putzig, N. E., Mattei, S., et al. (2009). Dielectric properties of lava flows west of Ascraeus Mons, Mars. *Geophysical Research Letters*, *36*(23), L23204. https://doi.org/10.1029/2009gl041234

Casademont, T. M., Eide, S., Shoemaker, E. S., Liu, Y., Nunes, D. C., Russell, P., et al. (2023). RIMFAX ground penetrating radar reveals dielectric permittivity and rock density of shallow Martian subsurface. *Journal of Geophysical Research: Planets*, *128*, e2022JE007598. https://doi.org/10.1029/2022JE007598

Ding, C., Xiao, Z., Su, Y., Zhao, J., & Cui, J. (2020). Compositional variations along the route of Chang'e-3 Yutu rover revealed by the lunar penetrating radar. *Progress in Earth and Planetary Science*, *7*(1), 1–11. https://doi.org/10.1186/s40645-020-00340-4

Economou, N., & Kritikakis, G. (2016). Attenuation analysis of real GPR wavelets: The equivalent amplitude spectrum (EAS). *Journal of Applied Geophysics*, *126*, 13–26. https://doi.org/10.1016/j.jappgeo.2016.01.005

Eide, S., Casademont, T., Aardal, Ø. L., & Hamran, S.-E. (2022). Modeling FMCW radar for subsurface analysis. *IEEE Journal of Selected Topics in Applied Earth Observations and Remote Sensing*, *15*, 2998–3007. https://doi.org/10.1109/JSTARS.2022.3165135

Farley, K. A., Stack, K. M., Shuster, D. L., Horgan, B. H. N., Hurowitz, J. A., Tarnas, J. D., et al. (2022). Aqueously altered igneous rocks sampled on the floor of Jezero Crater, Mars. *Science*, *0*(0), eabo2196. https://doi.org/10.1126/science.abo2196

Gambacorta, L., Raguso, M. C., Mastrogiuseppe, M., & Seu, R. (2022). UWB processing applied to multifrequency radar sounders: The case of MARSIS and comparison with SHARAD. *IEEE Transactions on Geoscience and Remote Sensing*, *60*, 1–14. https://doi.org/10.1109/TGRS.2022.3216893

Giannakis, I., & Giannopoulos, A. (2014). A novel piecewise linear recursive convolution approach for dispersive media using the finite-difference time-domain method. *IEEE Transactions on Antennas and Propagation*, *62*(5), 2669–2678. https://doi.org/10.1109/TAP.2014.2308549

Hamran, S.-E., & Paige, D. A. (2021). Mars 2020 perseverance rover RIMFAX raw and calibrated data products [Dataset]. NASA PDS Geosciences Node. Retrieved from https://pds-geosciences.wustl.edu/missions/mars2020/rimfax.htm

Hamran, S.-E., Paige, D. A., Allwood, A., Amundsen, H. E. F., Berger, T., Brovoll, S., et al. (2022). Ground penetrating radar observations of subsurface structures in the floor of Jezero Crater, Mars. *Science Advances*, *8*(34), eabp8564. https://doi.org/10.1126/sciadv.abp8564

Hamran, S.-E., Paige, D. A., Amundsen, H. E., Berger, T., Brovoll, S., Carter, L., et al. (2020). Radar imager for Mars' subsurface experiment—RIMFAX. *Space Science Reviews*, *216*(8), 1–39. https://doi.org/10.1007/s11214-020-00740-4

Harbi, H., & McMechan, G. A. (2012). Conductivity and scattering q in GPR data: Example from the ellenburger dolomite, central Texas. *Geophysics*, *77*(4), H63–H78. https://doi.org/10.1190/geo2011-0337.1

Irving, J. D., & Knight, R. J. (2003). Removal of wavelet dispersion from ground-penetrating radar data. *Geophysics*, *68*(3), 960–970. https://doi.org/10.1190/1.1581068

Jonscher, A. K. (1977). The "universal" dielectric response. *Nature*, *267*(5613), 673–679. https://doi.org/10.1038/267673a0

Larsen Greiner, T. A., Hlebnikov, V., Lie, J. E., Kolbjørnsen, O., Kjelsrud Evensen, A., Harris Nilsen, E., et al. (2020). Cross-streamer wavefield reconstruction through wavelet domain learning. *Geophysics*, *85*(6), V457–V471. https://doi.org/10.1190/geo2019-0771.1

Lauro, S. E., Baniamerian, J., Cosciotti, B., Mattei, E., & Pettinelli, E. (2022). Loss tangent estimation from ground-penetrating radar data using Ricker wavelet centroid-frequency shift analysis. *Geophysics*, *87*(3), H1–H12. https://doi.org/10.1190/geo2021-0431.1

Madsen, M. B., Goetz, W., Bertelsen, P., Binau, C. S., Folkmann, F., Gunnlaugsson, H. P., et al. (2009). Overview of the magnetic properties experiments on the Mars exploration rovers. *Journal of Geophysical Research*, *114*(E6), E06S90. https://doi.org/10.1029/2002je002029

Olhoeft, G. R., & Strangway, D. (1975). Dielectric properties of the first 100 meters of the moon. *Earth and Planetary Science Letters*, *24*(3), 394–404. https://doi.org/10.1016/0012-821x(75)90146-6

Oudart, N., Ciarletti, V., Le Gall, A., Mastrogiuseppe, M., Hervé, Y., Benedix, W.-S., et al. (2021). Range resolution enhancement of wisdom/exomars radar soundings by the bandwidth extrapolation technique: Validation and application to field campaign measurements. *Planetary and Space Science*, *197*, 105173. https://doi.org/10.1016/j.pss.2021.105173

Quan, Y., & Harris, J. M. (1997). Seismic attenuation tomography using the frequency shift method. *Geophysics*, *62*(3), 895–905. https://doi.org/10.1190/1.1444197

Richards, P. G., & Aki, K. (1980). *Quantitative seismology: Theory and methods* (Vol. 859). Freeman.

Simon, M. N., Carter, L. M., Campbell, B. A., Phillips, R. J., & Mattei, S. (2014). Studies of lava flows in the THARSIS region of Mars using SHARAD. *Journal of Geophysical Research: Planets*, *119*(11), 2291–2299. https://doi.org/10.1002/2014je004666

Stillman, D. E., & Grimm, R. E. (2011). Radar penetrates only the youngest geological units on Mars. *Journal of Geophysical Research*, *116*(E3), E03001. https://doi.org/10.1029/2010je003661

Stillman, D. E., & Olhoeft, G. (2008). Frequency and temperature dependence in electromagnetic properties of Martian analog minerals. *Journal of Geophysical Research*, *113*(E9), E09005. https://doi.org/10.1029/2007je002977

Tonn, R. (1991). The determination of the seismic quality factor Q from VSP data: A comparison of different computational methods. *Geophysical Prospecting*, *39*(1), 1–27. https://doi.org/10.1111/j.1365-2478.1991.tb00298.x

Turner, G., & Siggins, A. F. (1994). Constant Q attenuation of subsurface radar pulses. *Geophysics*, *59*(8), 1192–1200. https://doi.org/10.1190/1.1443677

Ulaby, F. T., & Long, D. G. (2014). Microwave radar and radiometric remote sensing. (Vol. *4*). University of Michigan Press

Ulaby, F. T., Bengal, T. H., Dobson, M. C., East, J. R., Garvin, J. B., & Evans, D. L. (1990). Microwave dielectric properties of dry rocks. *IEEE Transactions on Geoscience and Remote Sensing*, *28*(3), 325–336. https://doi.org/10.1109/36.54359

Van Der Baan, M. (2001). Acoustic wave propagation in one dimensional random media: The wave localization approach. *Geophysical Journal International*, *145*(3), 631–646. https://doi.org/10.1046/j.1365-246x.2001.01405.x

Warren, C., Giannopoulos, A., & Giannakis, I. (2016). gprMax: Open source software to simulate electromagnetic wave propagation for Ground Penetrating Radar. *Computer Physics Communications*, *209*, 163–170. https://doi.org/10.1016/j.cpc.2016.08.020

Wiens, R. C., Udry, A., Beyssac, O., Quantin-Nataf, C., Mangold, N., Cousin, A., et al. (2022). Compositionally and density stratified igneous terrain in Jezero Crater, Mars. *Science Advances*, *8*(34), eabo3399. https://doi.org/10.1126/sciadv.abo3399